RADAR OBSERVATIONS FROM THE HAYSTACK ULTRAWIDEBAND SATELLITE IMAGING RADAR IN 2019

James Murray[(1)], Timothy Kennedy[(2)], Mark Matney[(2)], Rossina Miller[(1)]

[(1)]Jacobs, NASA Johnson Space Center, 2101 NASA Pkwy XI5-9E, Houston, TX 77058, USA,
james.i.murray@nasa.gov
[(2)]NASA Johnson Space Center, 2101 NASA Pkwy XI511, Houston, TX 77058, USA

ABSTRACT

The NASA Orbital Debris Program Office (ODPO) conducts radar measurements of the low Earth orbit (LEO) orbital debris environment on a continual basis for monitoring and to enable modeling of the environment over time. Radar observations from the Haystack Ultrawideband Satellite Imaging Radar (HUSIR) in 2019 are the most recent snapshot of the environment to date that has been both measured and analyzed. HUSIR provides data on orbital debris in LEO down to a NASA size estimation model (SEM) size of approximately 5.5 mm, depending upon altitude and year-to-year variation in the sensitivity of the radar. This is of interest as it is the millimeter-sized orbital debris that drives mission-ending risk to robotic spacecraft in LEO. This paper will explore the results of the 2019 HUSIR radar measurements, including above-average flux measurements at lower LEO altitudes and the evolution of the flux during the time of observations.

1 INTRODUCTION

The NASA Orbital Debris Program Office (ODPO) relies primarily on ground-based radar measurements to characterize the distribution of small debris in low Earth orbit (LEO), down to approximately 3 mm depending upon altitude and the sensor used. Since the early 1990's, the Massachusetts Institute of Technology (MIT) Lincoln Laboratory (LL) has been collecting radar measurements for the NASA ODPO under agreements with the U.S. Department of Defense [1]. The Haystack Ultrawideband Satellite Imaging Radar (HUSIR) is the primary ground-based radar sensor used by the ODPO, and provides data on orbital debris (OD) down to approximately 5.5 mm below 1000 km altitude under nominal operating conditions for this sensor, where size is calculated using the NASA size estimation model (SEM). Since OD of this size are a significant risk to both human spaceflight and robotic missions in LEO, the sensitivity of this radar makes it a high-value sensor in understanding the distribution of OD at smaller sizes than are available from the public Space Surveillance Network (SSN) catalog, which is considered complete down to approximately 10 cm in LEO.

Radar measurements are conducted on a continual basis for OD environmental monitoring and modeling of the environment over time. HUSIR observations from 2019 are the most recent snapshot of the environment that has been both measured and analyzed to date from this sensor. In 2019, several interesting events happened on-orbit, including the start of large constellation deployments into LEO, as well as the Indian anti-satellite (ASAT) collision test with Microsat-R (International Designator 2019-006A, U.S. Space Command (USSPACECOM) Space Surveillance Network (SSN) catalog number 43947). Due to these events, coupled with a general increase in the number of missions and participants launching missions in recent years, continual monitoring is necessary to determine the effects of this increased activity on the OD environment. This paper will explore the results of the 2019 HUSIR radar measurements as compared to previous years of measurements, including above-average flux measurements at lower LEO altitudes and the evolution of the flux during the time of observations.

2 DATA COLLECTION OVERVIEW

The dataset presented in this report was collected during Calendar Year (CY) 2019 using the HUSIR radar. This radar is located in Tyngsborough, Massachusetts with a Cassegrain focus at 42.623287° N, 288.511846° E at an elevation of 115.69 m with respect to the 1984 World Geodetic System (WGS 84) Earth model [2 – 4]. Fig. 1 shows a photo of HUSIR, inside its geodesic radome on the left, next to the smaller Haystack Auxiliary Radar (HAX) on the right.

Figure 1. Photo of the HUSIR and HAX radars. Image reprinted with permission Courtesy of MIT Lincoln Laboratory, Lexington, Massachusetts.

The nominal sensitivity of HUSIR is 59.2 dB where sensitivity is defined as the single pulse signal-to-noise ratio (SNR) for an object with a radar cross section (RCS)

Proc. 8th European Conference on Space Debris (virtual), Darmstadt, Germany, 20–23 April 2021, published by the ESA Space Debris Office
Ed. T. Flohrer, S. Lemmens & F. Schmitz, (http://conference.sdo.esoc.esa.int, May 2021)

of one square meter at 1000 km slant range. The actual sensitivity can vary, mostly due to variations in transmission power which must be taken into account when comparing datasets across years. Fig. 2 shows the sensitivity history of HUSIR for OD radar observations during CY2019. The dashed black line in Fig. 2 indicates the nominal sensitivity for HUSIR, while the data points indicate measured sensitivity in 2019. The sensitivity was lower than nominal due to several maintenance issues that occurred during CY2019 related to HUSIR's travelling wave tubes [4].

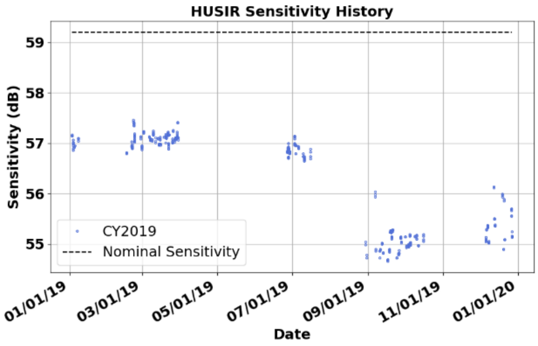

Figure 2. Sensitivity history for HUSIR in CY2019.

For OD radar measurements, HUSIR operates in a beam-park mode in which the radar stares at a specific topocentric azimuth and elevation angle for the duration of the observation. This provides a fixed detection volume that simplifies calculations of the debris flux, or number of objects detected per unit area, per unit time. Since the radar does not change its pointing in beam-park mode, and the radar beam has a 0.058° two-sided, 3 dB beamwidth, the observation time is short and relatively few pulses are collected on each object. Although this limits the precise measurement of a detected object's orbital parameters, the pointing geometry can be utilized to provide meaningful orbital information.

The data presented here was taken staring at an azimuth of 90° (due East) and an elevation of 75°, referred to as 75E. By staring just off-zenith, the 75E pointing geometry allows the radar to measure Doppler shifts that give meaningful orbital information for orbital inclinations between approximately 40° inclination and 140° inclination, using a circular orbit approximation. The high-elevation angle of the 75E staring geometry also minimizes atmospheric attenuation, allowing the radar to detect very small debris objects in orbit. Additional data from this radar was collected at other orientations for specific campaigns, including low elevation staring south to observe lower inclination orbits – results from those campaigns are not included in this paper.

Tab. 2 presents a summary of the number of observation hours contained in the dataset and the number of detections observed from 2014 to 2019. The number of detections represents the total number of events for which there were three or more pulses with an integrated SNR greater than 5.65 dB, where at least one is in the two-way, 6 dB beamwidth (one-way, two-sided 3 dB-beamwidth). The observation hours and number of detections shown in Tab. 2 for 2019 is atypical for HUSIR – being less than usual – following several significant maintenance events, as well as an increase in detected radio frequency interference (RFI) that occurred in 2019. Despite this, a number of interesting events were observed by the radar, which are described in later sections of this paper.

Table 1. Data Collection Summary for 2014-2019 at 75E.

Year	Hours of Observation	Number of Detections
2014	268.1	4107
2015	288.4	4858
2016	458.5	7079
2017	496.2	5701
2018	313.2	4964
2019	116.2	1864

2.1 The NASA Size Estimation Model

The NASA SEM was developed to relate radar cross section (RCS), which is directly measured by the radar, to a model for the physical size of an on-orbit debris fragment. The NASA SEM makes use of a parameter referred to as an object's characteristic length. The characteristic length is defined as the average of the largest dimensions for an object measured along three orthogonal axes. The first axis was chosen to coincide with the largest dimension, the second axis to coincide with the largest dimension in a plane orthogonal to the first axis, and the third axis to be orthogonal to the plane defined by the first two axes. Here, the characteristic length of an object is referred to interchangeably with size or diameter. Additional details regarding the NASA SEM may be found in [5 – 7].

In Fig. 3 the results of RCS-to-size measurements of 39 representative debris objects are shown over the frequency range 2.0 – 18 GHz (15-1.67 cm wavelength), where each point represents an average RCS over many orientations for a single object measured at a single frequency. The oscillating blue curve is the RCS for a spherical conductor while the smooth black curve is the model fit to the data and comprises the NASA SEM.

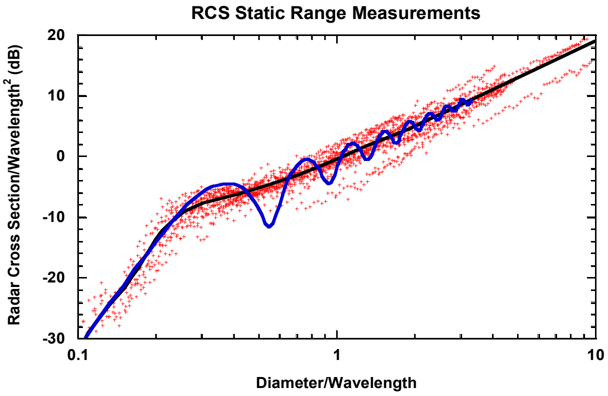

Figure 3. Results of RCS-to-physical size measurements of 39 representative debris objects. The oscillating line is the RCS for a spherical conductor while the smooth line is the model fit to the data.

3 ENVIRONMENT OVERVIEW

The radar data presented here provides a broad overview of the state of the debris environment in low Earth orbit over one CY. In the following sections recent data from CY2019 is compared to data taken by HUSIR during U.S. Government Fiscal Years (FY) 2014–2017, as well as CY2018. Note that in CY2018 the ODPO Radar Measurements team transitioned from FY to CY basis reporting to make comparisons to NASA's Orbital Debris Engineering Model (ORDEM) as well as other data sources easier. Since the radar sensitivity changes from year-to-year, flux charts presented in this section, which compare many years of data, may be presented to either a limiting size or a limiting altitude – depending upon the context of the quantities being plotted.

3.1 SEM-size Cumulative Distribution

Due to fluctuations in radar sensitivity, the total count rate (number of detections/hour) of detected objects can change from year to year. The shape of the cumulative SEM size distribution, however, should remain largely the same down to the sensitivity limit of a particular year. Any major changes in the size distribution can indicate the underlying OD environment has changed. The cumulative size distributions for the FY2014–2017, CY2018, and CY2019 75E datasets collected by HUSIR are compared in Fig. 4. The shaded regions represent the 2σ Poisson uncertainties. There is a small dip between 7 mm and 2 cm in the CY2018 and CY2019 data relative to FY2014–2017. This is related to a signal processing change in the OPDO radar processing software between the FY2014–2017 datasets and CY2018–2019 datasets and is not indicative of a change in the OD environment. As described in [3, 4] the signal processing conducted in FY2014–2017 had the effect of slightly overestimating the SEM size assigned to OD detections with radar cross sections between approximately -40 dBsm and -35 dBsm, which for the HUSIR wavelength, reduces the cumulative size distribution for OD larger than 1 cm in CY2018–2019. This is discussed in greater detail in Section 3.2 of this paper.

In [3], it was shown that in CY2018, for sizes larger than approximately 7 cm, there was an increase in the count rate for these larger objects relative to previous years. It was determined that the total size distribution above 7 cm was skewed higher in CY2018 by a handful of very large detections at the large end of the distribution – with all but two correlating to objects in the public SSN catalog. Limiting the distribution to objects smaller than 1 m, as shown in Fig. 5, the SEM size distributions are better matched to each other in different years. Since CY2019 does not show this same increase in the size distribution for larger objects (> 7 cm), the increase observed in CY2018 appears to be a one-time event, and not indicative of a long-term change in the OD environment.

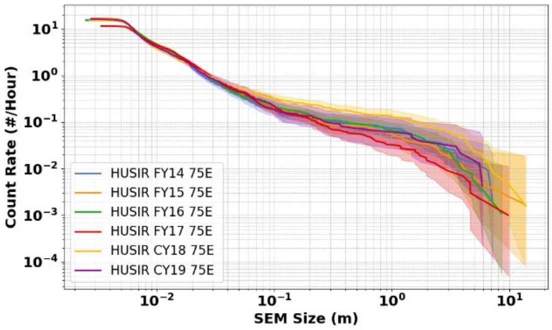

Figure 4. SEM-size Cumulative Distribution for all 75E data, by year. The shaded regions represent the 2σ uncertainty bounds.

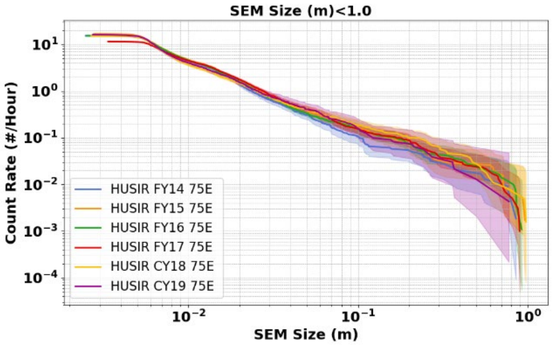

Figure 5. SEM-size Cumulative Distribution for all 75E data, by year, limited to objects less than 1 meter. The shaded regions represent the 2σ uncertainty bounds.

3.2 Surface Area Flux versus Altitude

Flux here is defined as the number of detections through the lateral surface area of the radar beam, considering the two-sided 3-dB beamwidth of the main beam only, within a given period of time. Total flux represents the flux of all objects regardless of SEM size. To aid in comparing different years, cumulative flux to a limiting size, i.e., objects with a given SEM size and larger, are shown in this section. For all years, cumulative flux is presented to limiting sizes of either 5.62 mm or 1 cm, depending upon altitude.

Fig. 6 shows the cumulative flux versus altitude for different years, limited to 1 cm, for HUSIR 75E observations. As discussed in [3], flux for CY2018 appears to be lower than previous years in many altitude bins. This is related to the previously mentioned signal processing change in more recent years, which reduces the total size distribution at 1 cm, this effect is also present in the CY2019 data and does not represent a change to the OD environment. In CY2019, the observed flux in the 1050–1100 km altitude bin appears significantly lower than previous years – more than expected from the signal processing change. Although the cause is not currently known, it may be the result of too few hours in CY2019. The large uncertainties for this bin in CY2019 overlap with uncertainties from earlier years – indicating that the difference observed is not statistically significant.

Fig. 7 shows the cumulative flux versus altitude for different years, limited to 5.62 mm, for HUSIR 75E observations. Here, CY2018 and CY2019 much more closely match previous years, since the processing software update does not affect the cumulative size distribution for sizes smaller than approximately 7 mm, as discussed in section 3.2.1 of [3]. An interesting feature present in both the 1 cm and 5.62 mm fluxes is an increase over previous years from 400 km to 700 km in altitude. Analysis has shown this increase is related to the ASAT weapons test performed against the Microsat-R satellite by India on 27 March 2019. This is discussed in greater detail in Section 4.

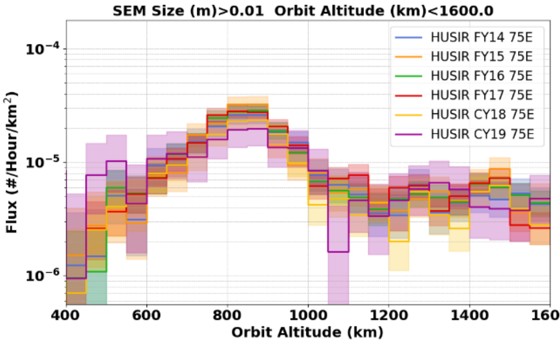

Figure 6. Cumulative surface area flux versus altitude limited to 1 cm for all 75E data, by year. The shaded regions represent the 2σ uncertainty bounds.

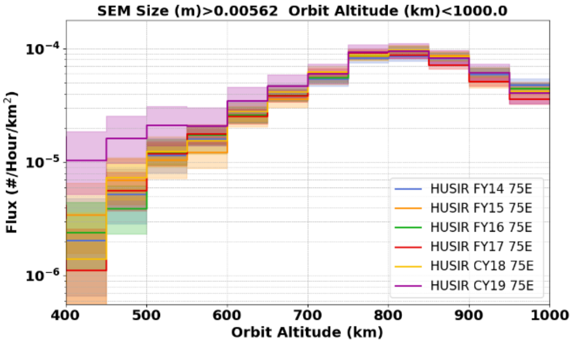

Figure 7. Cumulative surface area flux versus altitude limited to 5.62 mm for all 75E data, by year. The shaded regions represent the 2σ uncertainty bounds.

3.3 Surface Area Flux versus Inclination

Examination of flux versus inclination is described in this section to gain additional insight into the distinct populations/families of debris in LEO. Flux is defined in the same fashion as in previous sections, except that the beam area is the total surface area of the beam from the minimum observable altitude to the maximum observable altitude, since each altitude bin can measure debris at all inclinations observable by the radar in the 75E pointing geometry. Fluxes presented in this section are to limiting sizes of 5.62 mm and 1 cm and use 2-degree-sized bins.

Like the flux versus altitude charts, the flux for objects larger than 1 cm, as shown in Fig. 8, is lower in many inclination bins in both CY2018 and CY2019. In particular, between 64° and 68° the flux appears to be much lower than in previous years. The majority of debris in this inclination band belongs to the Sodium-Potassium (NaK) debris population. Due to the size distribution of NaK, which typically have more objects measured by HUSIR with radar cross sections between -40 and -35 dBsm, the effect of the signal processing change disproportionately affects the measured RCS distribution of this population.

Fig. 9 shows cumulative surface area flux versus inclination limited to 5.62 mm for all 75E data, by year. Like the flux versus altitude charts, the years appear to be much more consistent for this limiting size. This is likely due to the reduced uncertainty in the count rate of these smaller objects, as well as the signal processing change no longer having an effect on the cumulative results at this SEM-size and larger. In Fig. 9, although the flux is lower in CY2019, the uncertainties are still such that in many of the inclination bins, the results have overlapping uncertainties with other years. Hence, there is not statistical evidence that the results observed in CY2019 actually are different from other years for the 5.62 mm and larger population in these cases. There does appear to be a modest flux increase from 86° to 92° and near 44° to 46° inclination in CY2019. The flux increase between 86° and 92° is related to the increased low altitude flux described in Section 3.2, and will be discussed further in Section 4.

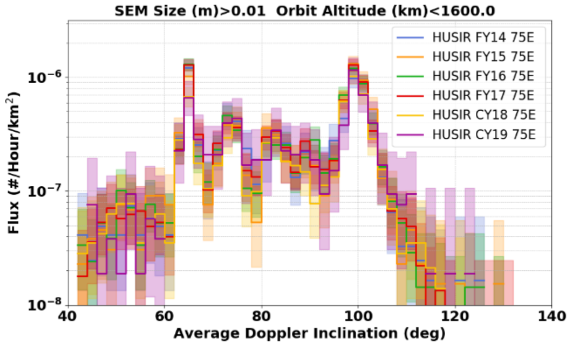

Figure 8. Cumulative surface area flux versus inclination limited to 1 cm for all 75E data, by year. The shaded regions represent the 2σ uncertainty bounds.

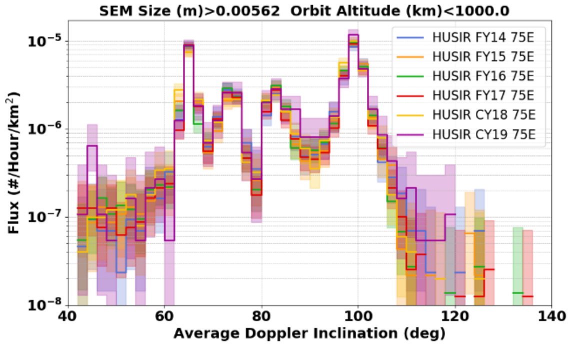

Figure 9. Cumulative surface area flux versus inclination limited to 5.62 mm for all 75E data, by year.The shaded regions represent the 2σ uncertainty bounds.

4 BREAKUP IDENTIFICATION

In an effort to determine the cause of the low altitude flux increase described in earlier sections of this paper, the detections between 400 km and 600 km in altitude were analyzed separately. Analysis of the low altitude cumulative size distribution showed that the distribution increased across a wide range of sizes potentially indicating a fragmentation event. A fragmentation event would also result in an increased debris flux for inclinations near the inclination of the parent body. Fig. 10 shows the low altitude flux versus Doppler inclination. There is a very clear increase between 80° to 88° and 104° to 114° Doppler inclination. In particular, no flux was measured in years prior to CY2019 between 104° and 114° Doppler inclination and between 400 km and 600 km in altitude.

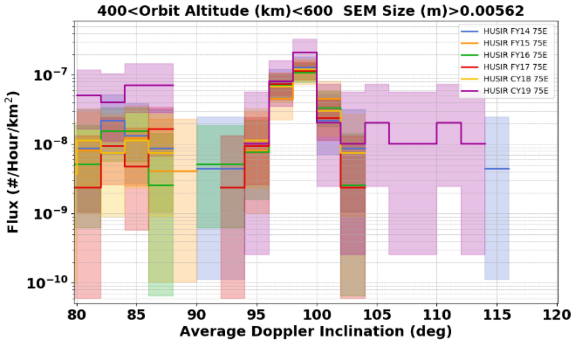

Figure 10. Cumulative surface area flux versus inclination limited to 5.62 mm for all 75E data, by year, altitude limited. The shaded regions represent the 2σ uncertainty bounds.

To determine if the increase was localized in time, the low altitude data was split into CY Quarters, as defined in Tab. 3 by day of year (DOY). Fig. 11 shows that the total count rate between 400 km and 600 km increased from Quarter 1 (Q1) to Quarter 2 (Q2), remained elevated from Q2 to Quarter 3 (Q3), and dropped back down from Q3 to Quarter 4 (Q4). Based on this analysis, the event likely occurred before DOY 182, but not much before DOY 91, in the Q2 time frame.

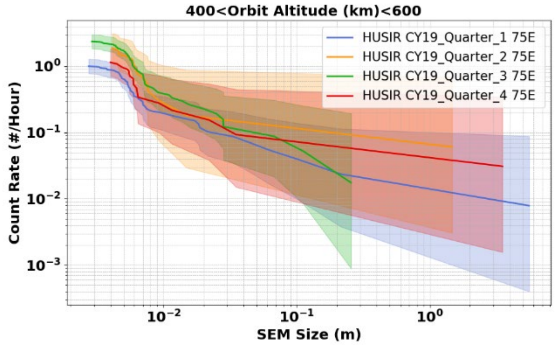

Figure 11. SEM-size Cumulative Distributions of CY2019 broken into CY quarters. The shaded regions represent the 2σ uncertainty bounds.

Table 2. Range of DOY associated with each CY2019 Quarter.

Quarter	Start DOY	Stop DOY
Q1	1	90
Q2	91	181
Q3	182	273
Q4	274	365

Table 3. All known breakups that occurred in or near CY2019.

SATELLITE NAME	BREAKUP YEAR	BREAKUP DOY	APOGEE (KM)	PERIGEE (KM)	INCLINATION (DEG)
ORBCOMM FM16	2018	356	783	780	45
MICROSAT-R	2019	86	294	265	96.63
USA 288 R/B	2019	96	35092	8526	12.2
LES 8,9/SOLRAD 11A,B R/B	2019	127	36889	35793	16.4
TOPEX-POSEIDON R/B	2019	203	1404	1296	66.07
COSMOS 2464-2466 ULLAGE MOTOR	2019	224	18907	541	65
COSMOS 2424-2426 ULLAGE MOTOR	2019	296	19189	294	64.5
COSMOS 2491	2019	357	1517	1485	82.5
COSMOS 2456-2458 ULLAGE MOTOR	2019	355-357	18980	512	64.7

Tab. 4 contains information on all breakups known to have occurred in and near CY2019. Of the nine events listed, only the first three of CY2019 occurred within the proper time frame; Microsat-R on DOY 86, USA 288 R/B on DOY 96, and LES 8,9/SOLRAD 11A,B R/B on DOY 127. The perigee altitude of both rocket body breakups occurred much higher than is visible by HUSIR, leaving Microsat-R as the most likely candidate.

4.1 Microsat-R

The Indian Spacecraft Microsat-R (International Designator 2019-006A, SSN catalog number 43947) was launched on 24 January 2019. On 27 March 2019 it was intentionally destroyed in a test of a ground-based, direct-ascent ASAT weapon system. At the time of the breakup, the spacecraft was in an approximately 294 x 265 km altitude, 96.63° orbit [8]. As of 30 July 2020, a total of 129 fragments associated with the Microsat-R breakup entered the public satellite catalog, of which 10 fragments remained on-orbit. Although only 129 fragments entered the public catalog, over 400 fragments were initially tracked by SSN sensors. Fig. 12 shows the apogee and perigee altitudes versus orbital inclination of the 129 Microsat-R fragments that entered the catalog. Although these fragments have apogee altitudes as high as 1500 km and could potentially be seen by HUSIR, the orbital inclinations do not match the inclination bands with increased flux identified in Fig. 10. It should be noted; however, that the radar in beam-park mode does not measure inclination directly. Using a circular orbit approximation, and the range and range-rate measured by the radar, a Doppler inclination is inferred for an object. An object with an eccentric orbit will have a Doppler inclination that differs from the true inclination, and further analysis has shown the increased flux in Figs. 5 - 9 is likely attributable to Microsat-R.

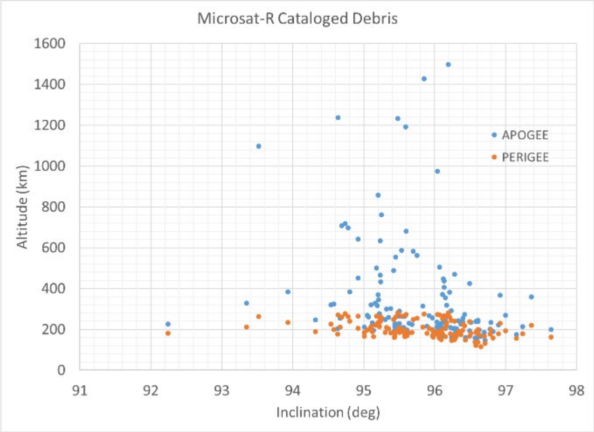

Figure 12. Apogee/Perigee altitudes versus orbital inclination of the 129 cataloged Microsat-R fragments.

In order to identify detections which are likely related to the Microsat-R breakup, a model cloud was simulated using NASA's Standard Satellite Breakup Model (SSBM). The SSBM is described in detail in [9]. For some time after a breakup, the fragments in a debris cloud remain grouped together in similar orbit planes. As the cloud moves through the field of view of the radar it generates a unique three-dimensional time, range, and range-rate pattern providing a means for correlating radar detections to debris clouds.

Once the model cloud was generated, the resulting modeled fragments were propagated to the HUSIR CY2019 observation window times between DOY 177 and 197 to determine the range and range-rate distribution of the modeled cloud, and whether there were observation opportunities for HUSIR during those time windows. This time period was chosen for an initial look because DOY 177 was the first observation time in the dataset after the breakup while DOY 197 is the last observation in the dataset before DOY 241. Propagation was performed using Prop3D [10], a long-term orbital element propagator that includes sun-moon, J2, J3, and J4 drag perturbations. Figs. 12 and 13 show the range and range-rate versus time distributions respectively of the modeled cloud for the HUSIR observation windows on DOY197. The start and stop times of the three observation windows are indicated by vertical lines. The red dots correspond to actual detections from HUSIR during these observation windows. Additionally, the predicted range and range-rate of cataloged Microsat-R debris for these observation windows are included in black.

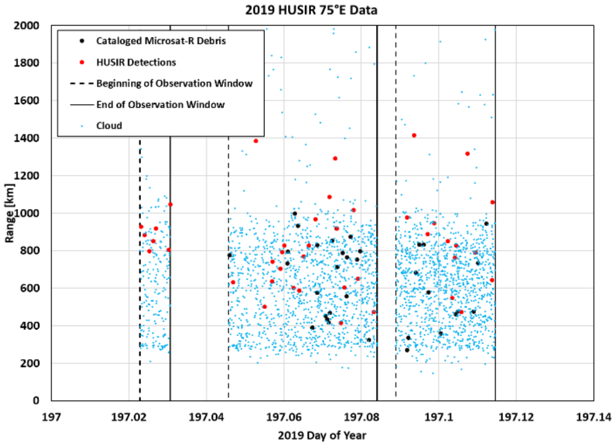

Figure 13. Range and time distribution of modeled Microsat-R debris, cataloged Microsat-R debris, and HUSIR detections for DOY 197.

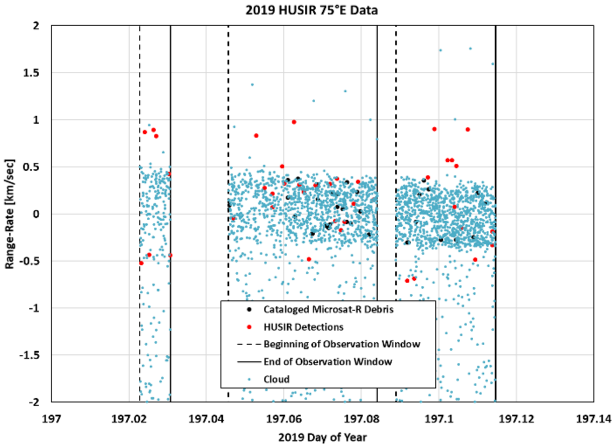

Figure 14. Range-rate and time distribution of modeled Microsat-R debris, cataloged Microsat-R debris, and HUSIR detections for DOY 197.

Fig. 15 summarizes the data from Figs. 13 and 14 in range and range-rate space. As can be seen in the figure, the modeled cloud forms a distinctive pattern against which we can compare actual HUSIR detections for the identification of Microsat-R debris in the HUSIR dataset.

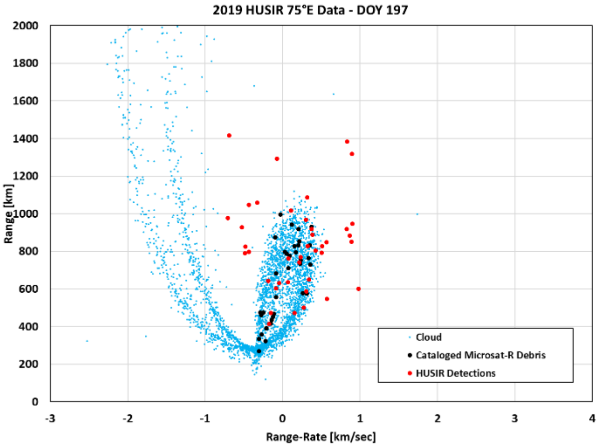

Figure 15. Range and range-rate distribution of modeled Microsat-R debris, cataloged Microsat-R debris, and HUSIR detections for DOY 197.

To correlate HUSIR detections with the modeled clouds, the publicly available density-based spatial clustering of applications with noise (DBSCAN) [11, 12] clustering algorithm was employed. DBSCAN performed better for this application than other clustering algorithms, such as k-means and Gaussian Mixture Modeling, due to its ability to handle the non-linearly separable and unique shape of the breakup cloud in range and range-rate space. DBSCAN also incorporates the concept of noise, making the algorithm more robust to outliers. DBSCAN uses two tunable parameters for assigning clusters, MinSamp (minimum number of samples for a cluster) and ε (parameter specifying radius of group), which control the density and distance metric properties used by the algorithm in finding clusters.

HUSIR detections were correlated to the modeled cloud by applying the clustering algorithm on a combination of the modeled cloud and actual HUSIR data. HUSIR detections that were clustered with the modeled cloud data were flagged as Microsat-R debris, leaving the noise points, as determined by DBSCAN, as the background debris data. Since the shape of the modeled cloud in range and range-rate space is variable over time, this clustering identification was performed for each DOY for which the cloud was modeled. Fig. 16 shows the results of the clustering for each DOY where blue points indicate the cluster identified for the modeled cloud data and the red points represent HUSIR detections. Points that were determined to be noise – not part of a cluster – are denoted with an “x”. The red points denoted with circles in the figure were HUSIR observations flagged as correlated with Microsat-R debris. Note that the black points are also part of the original modeled cloud dataset; however, they are located in less dense regions of the cloud in range and range-rate space.

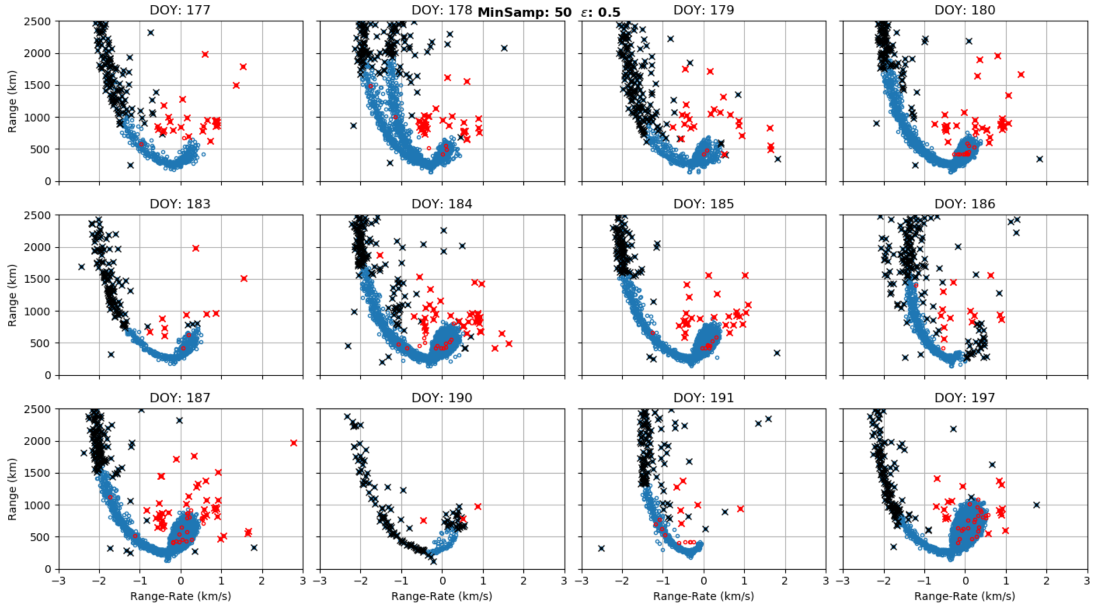

Figure 16. Results of the DBSCAN clustering algorithm on a DOY basis. The two tunable parameters for DBSCAN are minimum samples for a cluster (MinSamp = 50) and neighborhood size (ε = 0.5).

DBSCAN parameters were chosen, MinSamp= 50 and ε = 0.5, such that HUSIR observations having similar range and range-rate values to the more densely populated regions of the cloud could be readily identified. This resulted in some of the cloud points in more sparsely populated regions being excluded by the algorithm. Although there are some cases where the application of the algorithm could be refined, its overall performance in identifying HUSIR points correlated with the cloud is sufficient to demonstrate the effects of the cloud on the altitude and inclination flux distributions.

Fig. 17 shows the cumulative surface area flux versus altitude limited to 5.62 mm for all years, as well as for the CY2019 data with detections flagged as Microsat-R debris removed. The flux from 400 km to 600 km in altitude has been reduced significantly. The resulting data is now statistically equivalent to previous years in the 400 km to 450 km bin and the 550 km to 600 km bin. The flux is still slightly elevated, though significantly reduced, from 450 km to 550 km, although the uncertainties are still overlapping with the other years to a large extent. One possible explanation for this is that the analysis thus far has only attempted to filter the HUSIR data from DOY 177 to DOY 197 and the residual elevated altitude flux is related to Microsat-R debris detected outside of this time span. This could be exacerbated by lower aerodynamic drag in the current solar minimum. While additional work is currently underway to apply this process to the entirety of the CY2019 dataset, current results are sufficient to state that debris from the Microsat-R ASAT test are likely the primary contributor to the changes seen in the altitude and inclination fluxes when compared to previous years.

Fig. 18 shows the cumulative surface area flux versus Doppler inclination limited to 5.62 mm for all years as well as for the CY2019 data with the detections flagged as Microsat-R debris removed. The flux in the 80° to 88° and 104° to 114° inclination bands, previously elevated, are now statistically equivalent to data in previous years after the removal of detections correlated with Microsat-R debris. Flux in the 44° to 46° inclination band, however, is still elevated in Fig. 18. Analysis of the altitude distribution of debris in the 44° to 46° inclination band shows an increase in flux at several altitudes, including from 450 km to 550 km, providing another possible explanation for the residual altitude flux increase. Additional analysis of this inclination band, which identifies ORBCOMM FM-16 as a possible source, is discussed in Section 4.2.

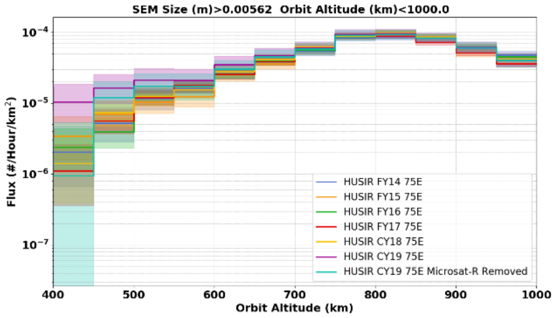

Figure 17. Cumulative surface area flux versus altitude limited to 5.62 mm for all 75E data, by year. Additionally, HUSIR CY2019 with the identified Microsat-R debris removed is shown.

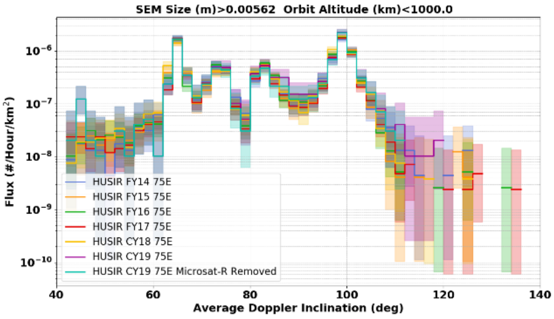

Figure 18. Cumulative surface area flux versus inclination limited to 5.62 mm for all 75E data, by year. Additionally, HUSIR CY2019 with the identified Microsat-R debris removed is shown.

4.2 ORBCOMM FM-16

After identifying and removing detections correlated with Microsat-R debris from the CY2019 data, there remains a flux increase over previous years in the 44° to 46° inclination band. Re-examination of Tab. 4 shows that a breakup occurred late in CY2018 at an inclination of 45°. On 22 December 2018, the ORBCOMM FM-16 spacecraft (International Designator 1998-046E, SSN catalog number 25417) experienced a debris generating event in a 783 × 782 km, 45° orbit [13]. Potential sources of the energetic fragmentation event include a gaseous nitrogen thruster system and batteries. Although 45 pieces initially were tracked by the SSN, only 12 pieces entered the public SSN catalog close to the time of the event, with a 13th being associated to the parent body in April 2020. Analysis of the inclinations of these tracked objects showed a maximum inclination change of 0.5° from the parent body, almost exclusively in the positive direction [14]. The initial orbital elements of these objects exhibited perigee altitudes as low as 400 km and apogee altitudes as high as 1500 km. Many of the objects, however, retained perigee altitudes near that of the parent body.

Fig. 19 shows the cumulative surface area flux versus altitude limited to SEM sizes of 5.62 mm and larger for all HUSIR 75E data, by year within the 44° to 46° inclination band. Note that the CY2019 HUSIR data with and without Microsat-R debris are identical in Fig. 19, and due to the order in which the data is plotted, results in only the curve for the CY2019 data without Microsat-R debris being readily identifiable. There is a significant increase in the 750 km to 800 km altitude bin. Although the flux appears higher at all altitudes, the uncertainties are large due to the low number of total counts in this inclination band, 20 total in CY2019. Although not definitive, evidence thus far indicates that the ORBCOMM FM-16 fragmentation event is a likely source of the 44° to 46° inclination flux seen in the HUSIR CY2019 data, and future investigation of this event using a similar methodology to that conducted in Section 4.1 for correlation with Microsat-R debris is of interest.

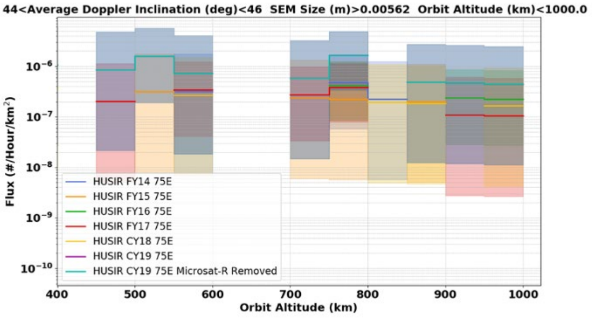

Figure 19. Cumulative surface area flux versus altitude limited to 5.62 mm for all 75E data, by year from 44° to 46° inclination. Data from HUSIR in CY2019 with detections that are correlated with Microsat-R debris removed is also shown.

5 SUMMARY

The LEO environment as observed and measured by the HUSIR OD radar in CY2019 was discussed and analyzed. A total of 116 observation hours were processed and analyzed from HUSIR. Detected objects were measured for RCS, range, and range-rate, and polarization. These data were analyzed to produce orbital altitude and inclination, size, and flux distributions.

Cumulative size distributions for FY2014–2017 and CY2018, were compared to the most recently analyzed CY2019 dataset – providing an overview of the state and evolution of the LEO environment. Although there was some year-to-year variation observed, e.g., an apparent increase in the CY2018 cumulative size distribution for objects larger than 7 cm, in general the cumulative size distributions are relatively similar across years of HUSIR radar measurements.

Surface area flux versus altitude and surface area flux versus inclination for FY2014–2017, CY2018, and CY2019 were also compared to provide additional insight into the evolution of different OD families. A significant increase in the flux from 400 km to 600 km in altitude was observed in 2019 relative to prior years. The most likely cause was shown to be from the breakup of the Microsat-R satellite as the result of an ASAT weapons test. A method for identifying HUSIR detections correlated with Microsat-R debris was developed utilizing a modeled breakup cloud generated by the NASA SSBM. These correlated detections were flagged and shown to be the major source of the flux increase. An additional flux increase between 44° to 46° inclination was also observed. A hypothesized cause is the ORBCOMM FM-16 debris generating event, and a future, more detailed investigation is of interest.

This paper presented key results from the curated CY2019 HUSIR radar measurements of the OD environment. HUSIR is the primary LEO OD data source that bridges the gap in size coverage from the SSN catalog down to SEM sizes of approximately 5.5 mm – depending on altitude and year-to-year sensitivity variation in the radar – used in development of NASA's OD models. Continued monitoring of the environment in the size ranges efficiently measured by HUSIR is needed to continue updating, validating, and refining these models. Further monitoring of the OD environment in size regimes smaller than SSN trackability is needed to assess the potential increased risk of collisions to critical assets in LEO.

6 ACKNOWLEDGEMENTS

The authors wish to thank Dr. Phillip Anz-Meador for his significant contributions in modeling the Microsat-R debris cloud and making the data available for analysis.

7 REFERENCES

1. Stansbery, E.G., Pitts, C.C., et al. (1991). Size and Orbit Analysis of Orbital Debris Data Collected using the Haystack Radar. JSC-25245, NASA Johnson Space Center, Houston, TX, USA.
2. Horstman, M.F., Papanyan, V.O., et al. (2014). Haystack and HAX Radar Measurements of the Orbital Debris Environment: 2006 – 2012. NASA/TP-2014-217391, NASA Johnson Space Center, Houston, TX, USA.
3. Murray, J. & Kennedy, T. (2020). Haystack Ultra-Wideband Satellite Imaging Radar Measurements of the Orbital Debris Environment: 2018. NASA/TP-2020-5006606, NASA Johnson Space Center, Houston, TX, USA.
4. Murray, J. & Kennedy, T. (In Work). Haystack Ultra-Wideband Satellite Imaging Radar Measurements of the Orbital Debris Environment: 2019. NASA Johnson Space Center, Houston, TX, USA.
5. Bohannon, G., Caampued, T., & Young, N. (1994). First Order RCS Statistics of Hypervelocity Impact Fragments. XonTech Report 940128-BE-2305.
6. Xu, Y.-l & Stokely, C.L. (2005). A Statistical Size Estimation Model for Haystack and HAX Radar Detections. *56th International Astronautical Congress*, Fukuoka, Japan.
7. Bohannon, G. & Young, N. (1993). Debris Size Estimating Using Average RCS Measurements. XonTech Report 930781-BE-2247.
8. Two Breakup Events Reported. (2019). *Orbital Debris Quarterly News, Vol. 23, Issue 3*, pp1.
9. Johnson, N.L., Krisko, P.H., et al. (2001). NASA's New Breakup Model of EVOLVE 4.0. *Adv. Space Res., 28* (9), 1377-1384.
10. Hall, D.T. (2004). PROP3D - a long-term, intermediate-accuracy orbital element propagator for space debris studies. NASA Internal Document.
11. Ester, M., Kriegel, H., et al. (1996). A density-based algorithm for discovering clusters in large spatial databases with noise. *Proceedings of the Second International Conference on Knowledge Discovery and Data Mining (KDD-96)*. AAAI Press, pp226-231.
12. Pedregosa, F., Varoquaux, G., et al. (2011). Scikit-learn: Machine Learning in Python. *Journal of Machine Learning Research* 12, pp2825-2830.
13. 2018 Ends with Breakup of an ORBCOMM Constellation Spacecraft. (2019). *Orbital Debris Quarterly News, Vol. 23, Issues 1 & 2*, pp1.
14. Peterson, G., Sorge, M., McVey, J. (2019). Forensic Analysis of Debris-Generating Events: Orbcomm FM 16. *1st International Orbital Debris Conference*, Sugar Land, TX, USA.